

Study of the photon-induced formation and subsequent desorption of CH₃OH and H₂CO in interstellar ice analogs

R. Martín-Doménech¹, G. M. Muñoz Caro¹, and G. A. Cruz-Díaz^{1,2,3}

¹ Centro de Astrobiología (INTA-CSIC), Ctra. de Ajalvir, km 4, Torrejón de Ardoz, 28850 Madrid, Spain
e-mail: rmartin@cab.inta-csic.es

² NASA Ames Research Center, Moffett Field, Mountain View, CA 94035, USA

³ Bay Area Environmental Research Institute, Petaluma, CA 94952, USA

Received 21 December 2015 / Accepted 6 February 2016

ABSTRACT

Context. Methanol and formaldehyde are two simple organic molecules that are ubiquitously detected in the interstellar medium, in both the solid and gaseous phases. An origin in the solid phase and a subsequent nonthermal desorption into the gas phase is often invoked to explain their abundances in some of the environments where they are found. Experimental simulations under astrophysically relevant conditions have been carried out in the past four decades in order to find a suitable mechanism for that process.

Aims. In particular, photodesorption from pure methanol ice (and presumably from pure formaldehyde ice) has been found to be negligible in previous works, probably because both molecules are very readily dissociated by vacuum-UV photons. Therefore, we explore the in situ formation and subsequent photon-induced desorption of these species, studying the UV photoprocessing of pure ethanol ice, and a more realistic binary H₂O:CH₄ ice analog.

Methods. Experimental simulations were performed in an ultra-high vacuum chamber. Pure ethanol and binary H₂O:CH₄ ice samples deposited onto an infrared transparent window at 8 K were UV-irradiated using a microwave-discharged hydrogen flow lamp. Evidence of photochemical production of these two species and subsequent UV-photon-induced desorption into the gas phase were searched for by means of a Fourier transform infrared spectrometer and a quadrupole mass spectrometer, respectively. After irradiation, ice samples were warmed up to room temperature until complete sublimation was attained for detection of volatile products.

Results. Formation of CH₃OH was only observed during photoprocessing of the H₂O:CH₄ ice analog, accounting for ~4% of the initial CH₄ ice column density, but no photon-induced desorption was detected. Photochemical production of H₂CO was observed in both series of experiments. Formation of formaldehyde accounted for ≤45% conversion of the initial ethanol ice, but it could not be quantified during irradiation of the binary H₂O:CH₄ ice analogs. Photochemidesorption of formaldehyde, i.e., photon-induced formation on the ice surface and immediate desorption, was observed, with a yield of $\sim 6 \times 10^{-5}$ ($\frac{\text{molecules}}{\text{incident photon}}$) in the case of the pure ethanol ice experiments, and $\sim 4.4 \times 10^{-5}$ ($\frac{\text{molecules}}{\text{incident photon}}$) when the H₂O:CH₄ ice analogs were photoprocessed. Photoprocessing of the ice analogs lead to formation of other species. Some of them were also found to desorb upon UV irradiation.

Conclusions. While certain C-bearing species, in particular H₂CO, were found to desorb upon irradiation, nonthermal desorption of CH₃OH was not observed. So far, there is no experimental evidence of any efficient CH₃OH desorption induced by UV photons. On the other hand, the observed photon-induced desorption of H₂CO could account for the total formaldehyde abundance observed in the Horsehead photodissociation-dominated region.

Key words. ISM: molecules – ISM: clouds – methods: laboratory: molecular

1. Introduction

More than 180 molecules have been detected to date in the interstellar medium (ISM). Simple organic molecules (hydrogenated species with just one carbon atom and another heavy element) are proposed as precursors of more complex organic species with prebiotic interest (e.g., Charnley et al. 1992; Bernstein et al. 1995, 2002; Gerakines et al. 2001; Muñoz Caro et al. 2002; Muñoz Caro & Schutte 2003; Nuevo et al. 2006; Garrod et al. 2008; Muñoz Caro & Dartois 2009; Herbst & van Dishoeck 2009; Öberg et al. 2010). Two of the most studied simple organic molecules are CH₃OH and H₂CO.

These species are found in a variety of interstellar environments, such as molecular clouds and hot cores, and in comets inside our solar system, with abundances relative to H₂ ranging from 10⁻⁶ to 10⁻⁹ (see, e.g., Sutton et al. 1995; Wootten et al. 1996; Ceccarelli et al. 2000; Ehrenfreund et al. 2002; Maret et al. 2004; Smith et al. 2004; Young et al. 2004; Araya et al. 2007; Leurini et al. 2010; Bergman et al. 2011; Guzmán et al. 2011, 2013). The origin of CH₃OH and H₂CO is, however, not

yet fully understood. Pure gas-phase chemical models cannot always reproduce their observed abundances (Garrod et al. 2006; Geppert et al. 2006; Guzmán et al. 2011, 2013), and solid-phase chemistry, either on the surface of dust grains or in the ice mantles that accrete on top of them, must therefore play a role in their formation.

Methanol is present in the solid and gaseous phases of the ISM. Solid CH₃OH has been detected in interstellar ice in dense cores with an abundance of 5–12% relative to water (Boogert et al. 2011) and also in the cold envelopes around high and low-mass protostars with abundances ranging from 1% up to 30% relative to water (Dartois et al. 1999; Gibb et al. 2000, 2004; Boogert et al. 2008; Pontoppidan et al. 2008; Bottinelli et al. 2010). Its abundance in solar system comets is lower (0.2–7%, Mumma & Charnley 2011, and references therein). Gas-phase CH₃OH has been detected in dense cores and photodissociation-dominated regions (PDRs) with a typical abundance of $\sim 10^{-9}$ relative to H₂ (see, e.g., Bergman et al. 2011; Guzmán et al. 2011, 2013). This abundance is usually

higher in hot cores ($\sim 10^{-7}$, Öberg et al. 2014, and references therein). In dense cores and PDRs where thermal desorption is inhibited, gas-phase models fail to reproduce the abundance of CH_3OH . Therefore, formation of this species in the solid phase and subsequently nonthermal desorption into the gas phase needs to be invoked (Guzmán et al. 2011, 2013, and references therein).

It has been proposed that CH_3OH is formed by successive addition of H atoms to CO molecules on the surface of dust grains (Tielens & Whittet 1997; Watanabe & Kouchi 2002; Fuchs et al. 2009) or, alternatively, in the bulk of water-rich ices (e.g., Watanabe et al. 2003). However, Hiraoka et al. (2002, 2005) have claimed that this formation pathway cannot be the major source of methanol in the ISM, since the reaction rates are too slow. Watanabe et al. (2007) acknowledge that the contribution of photolysis mechanisms (see below) could not be negligible in molecular clouds. Therefore, energetic processing of CO molecules in a water-ice matrix without directly involving any addition of H atoms has been proposed as an alternative source of CH_3OH . For example, photolysis of $\text{H}_2\text{O}:\text{CO}$ ice analogs (Schutte et al. 1996), proton bombardment of $\text{H}_2\text{O}:\text{CO}$ ices (Hudson & Moore 1999), or electron irradiation of $\text{H}_2\text{O}:\text{CO}:\text{H}_2\text{O}$ layered ices (Yamamoto et al. 2004).

Equivalent formation pathways using $\text{H}_2\text{O}:\text{CH}_4$ ice analogs have also been proposed for the proton bombardment (Moore & Hudson 1998) and the electron irradiation mechanisms (Wada et al. 2006), suggesting that the contribution of this mechanism for the formation of methanol was at least comparable to the H atom grain surface reactions. In the present work we have explored the photolysis of $\text{H}_2\text{O}:\text{CH}_4$ ice analogs. Madzunkov et al. (2010) propose a completely different formation route by collision of superthermal O atoms with CH_4 molecules in a methane ice with an overcoat of CO molecules.

No UV-photon-induced desorption of CH_3OH was observed in Cruz-Díaz et al. (in prep.) during irradiation of a pure methanol ice, in contrast to what was previously reported in Öberg et al. (2009). The low CH_3OH photodesorption of $\leq 1.8 \times 10^{-4}$ molecules per incident photon found in UV irradiation experiments of pure methanol ices, probably due to the likely dissociation of CH_3OH molecules upon vacuum-UV-photon absorption, cannot account for the abundances of gas-phase methanol in cold regions, and formation followed by subsequent nonthermal desorption pathways must therefore be explored as an alternative.

Formaldehyde has also been detected in both solid and gaseous phases. Solid H_2CO has not been detected yet in dense cores (Mumma & Charnley 2011), but it is present with an abundance of 1–6% relative to water in the cold envelopes around high- and low-mass protostars (Keane et al. 2001; Maret et al. 2004; Dartois 2005; Boogert et al. 2008), while its abundance is a little lower in solar system comets (0.1–1%, Mumma & Charnley 2011, and references therein). Gas-phase H_2CO is also detected in dense cores and PDRs with a similar abundance to that of methanol (see, e.g., Guzmán et al. 2011, 2013) and in hot cores, probably after thermal evaporation of ice mantles (e.g., Wootten et al. 1996; Ceccarelli et al. 2000; Maret et al. 2004; Young et al. 2004; Araya et al. 2007). Although pure gas-phase models have been able to reproduce the abundance of H_2CO in dense cores, formation of this species on dust grains and subsequent (nonthermal) desorption is still needed to account for its abundance in low UV-field, illuminated PDRs (for example, the Horsehead PDR, see Guzmán et al. 2011, 2013, and references therein).

Most of the solid-phase formation pathways proposed for H_2CO are shared with CH_3OH , since the former is usually an intermediate product in the formation of the latter. Formaldehyde can thus be produced by successive addition of H atoms to CO molecules (Tielens & Hagen 1982; Hiraoka et al. 1994; Watanabe & Kouchi 2002; Fuchs et al. 2009). Madzunkov et al. (2009) report a similar formation route of H_2CO by collision of superthermal H atoms with CO molecules on a gold surface. Alternatively, photolysis (Schutte et al. 1996), proton bombardment (Hudson & Moore 1999), and electron irradiation (Yamamoto et al. 2004) of $\text{H}_2\text{O}:\text{CO}$ ice analogs have reported the formation of H_2CO as an intermediate product in the formation of methanol. Moore & Hudson (1998) and Wada et al. (2006) studied the proton bombardment and electron irradiation of $\text{H}_2\text{O}:\text{CH}_4$ ice analogs, respectively. Photolysis of these binary ice samples is studied in the present work, as mentioned above. Formaldehyde can also be produced from UV or soft X-ray irradiation of pure methanol ices (Öberg et al. 2009; Ciaravella et al. 2010, respectively). Collision of superthermal O atoms with CH_4 molecules also leads to the formation of H_2CO according to Madzunkov et al. (2010).

Nonthermal desorption from pure formaldehyde ices has not yet been reported, but a behavior similar to that of pure methanol irradiation can be expected. Nonthermal desorption of molecules in cold regions can be induced by UV photons, cosmic rays, or exothermic chemical reactions (products formed in the surface of dust grains can immediately desorb due to the exothermicity of the reaction, Garrod et al. 2007; Hocuk & Cazaux 2015). Experimental simulations dedicated to photoprocessing of ice analogs under astrophysically relevant conditions have revealed that UV-photon-induced desorption can take place through two different main mechanisms (see also Martín-Doménech et al. 2015; Cruz-Díaz et al., in prep., and references therein).

Photodesorption itself is an indirect desorption induced by electronic transitions (DIET) process where the energy provided by a UV photon to a molecule in the subsurface region of the ice is subsequently redistributed to surface molecules, which are able to break the intermolecular bonds and desorb into the gas phase (Rakhovskaia et al. 1995; Öberg et al. 2007; Muñoz Caro et al. 2010; Fayolle et al. 2011; Bertin et al. 2012, 2013). In this case, the desorbing molecules do not have to belong to the same species as the molecules absorbing the UV photons. Fillion et al. (2014) distinguish between DIET photodesorption, when both the absorbing and desorbing molecules belong to the same species, and indirect DIET photodesorption, when the molecule absorbing the UV photon is different from the molecule finally desorbing. In this paper the term DIET photodesorption is used to refer to both cases. This process therefore depends on both the composition and UV absorption spectra of the subsurface ice layers and the intermolecular bonds of molecules on the ice surface. Photochemidesorption, on the other hand, is the desorption of excited photofragments or photoproducts right after their formation on the surface of the ice (Martín-Doménech et al. 2015; Cruz-Díaz et al., in prep.), including non-DIET desorption processes previously reported in Fayolle et al. (2013) and Fillion et al. (2014). This mechanism allows UV-photon-induced desorption of species that are not able to photodesorb significantly by irradiation of the pure ices (e.g., CH_4 produced during CH_3OH irradiation, Cruz-Díaz et al., in prep.).

In the present work we have explored new UV-induced-formation pathways and subsequent desorption for CH_3OH and H_2CO . On one hand, we have followed a top-down approach, studying the UV photodissociation of a pure ethanol ice (solid $\text{C}_2\text{H}_5\text{OH}$ has been proposed as one of the possible carriers of

the 7.24 μm ice band; Schutte et al. 1999; Öberg et al. 2011). A bottom-up approach is represented by a more realistic binary $\text{H}_2\text{O}:\text{CH}_4$ ice analog, following the experiments already mentioned in this section.

This paper is organized as follows. Section 2 describes the experimental simulations performed. The results are presented in Sect. 3. The astrophysical implications are elucidated in Sect. 4, and the conclusions are summarized in Sect. 5.

2. Experimental

The experimental simulations have been performed using the InterStellar Astrochemistry Chamber (ISAC) at the Centro de Astrobiología (Muñoz Caro et al. 2010). The ISAC setup consists in an ultra-high-vacuum (UHV) chamber with a base pressure of about 4×10^{-11} mbar, similar to what is found in dense cloud interiors. Pure ethanol ices were grown by deposition of $\text{C}_2\text{H}_5\text{OH}$ vapor onto a diamond window at 8 K, achieved by means of a closed-cycle helium cryostat. At this temperature, ices are deposited as amorphous solids. We used $\text{C}_2\text{H}_5\text{OH}$ (liquid, 99.9%) in this series of experiments. Binary ice analogs were grown in the interior of the chamber by simultaneous deposition of H_2O vapor and CH_4 gas onto the same substrate at 8 K. The isotopolog $^{13}\text{CH}_4$ was used in similar experiments to confirm the results. The chemical components used in this series of experiments were H_2O (liquid, triply distilled), CH_4 (gas, Praxair 99.95%), and $^{13}\text{CH}_4$ (gas, Cambridge Isotope Laboratories 99.9%).

Ice samples were UV-irradiated using an F-type microwave-discharged hydrogen flow lamp (MDHL) from Ophos Instruments with a VUV-flux of $\approx 2 \times 10^{14}$ photons $\text{cm}^{-2} \text{s}^{-1}$ at the sample position, measured by $\text{CO}_2 \rightarrow \text{CO}$ actinometry (Muñoz Caro et al. 2010). The size of the region irradiated by the lamp coincides with the size of the substrate. The spectrum of the MDHL is similar to the secondary UV field of dense cloud interiors calculated by Gredel et al. (1989) and also to the diffuse interstellar UV field (Jenniskens et al. 1993; Muñoz Caro & Schutte 2003), as well as to the far-UV field of emission/reflection nebulae (France et al. 2005). It has been characterized previously by Chen et al. (2010, 2014). More information can be found in Cruz-Díaz et al. (2014), where a description of the vacuum-ultraviolet (VUV) spectrophotometer used in our setup to monitor the VUV flux is provided. The mean photon energy is 8.6 eV. A MgF_2 window is used as interface between the lamp and the chamber, leading to a cutoff at ~ 114 nm (10.81 eV).

The ice samples were monitored by in situ Fourier-transform infrared (FTIR) transmittance spectroscopy after deposition and after every irradiation period, using a Bruker Vertex 70 spectrometer equipped with a deuterated triglycine sulfate detector (DTGS). The IR spectra were collected with a spectral resolution of 2–4 cm^{-1} (most spectra were subsequently smoothed). Column densities of selected species in the ice were calculated from the IR spectra using the formula

$$N = \frac{1}{A} \int_{\text{band}} \tau_\nu \, d\nu, \quad (1)$$

where N is the column density in molecules cm^{-2} , τ_ν the optical depth of the absorption band, and A the band strength in $\text{cm} \text{molecule}^{-1}$, as derived from laboratory experiments (Table 1). Band strengths in Table 1 were measured for pure amorphous ices except for ethanol. The same values are usually adopted in ice mixtures, which introduces an uncertainty of about 20–30% (d’Hendecourt & Allamandola 1986). In the case of ethanol, the

Table 1. IR feature used to calculate the column density of selected ice components.

Molecule	Frequency (cm^{-1})	Band strength ($\text{cm} \text{molec}^{-1}$)
$\text{C}_2\text{H}_5\text{OH}$	1044	7.3×10^{-18a}
H_2O	3280	2.0×10^{-16b}
CH_4	1304	6.4×10^{-18c}
CH_3OH	1025	1.8×10^{-17d}
H_2CO	1720	9.6×10^{-18e}

Notes. Frequencies and band strengths for pure ices at 10 K, except for $\text{C}_2\text{H}_5\text{OH}$ (see text). ^(a) From Moore & Hudson (1998); ^(b) from Hagen (1981); ^(c) from d’Hendecourt & Allamandola (1986). The same value was used as an approximation for the experiments with $^{13}\text{CH}_4$; ^(d) from d’Hendecourt & Allamandola (1986); ^(e) from Schutte et al. (1996).

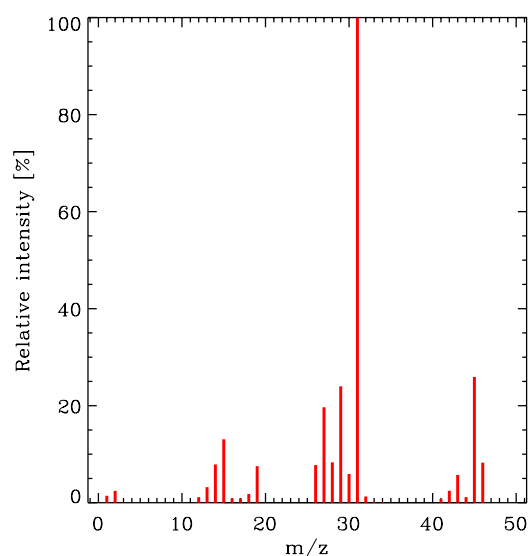


Fig. 1. Mass spectrum of ethanol in our setup.

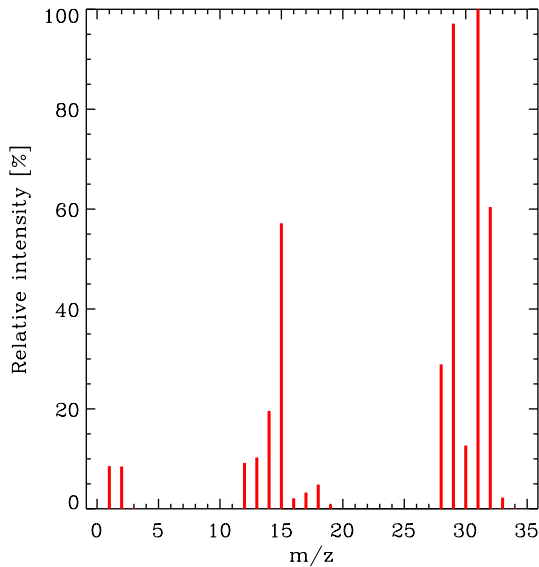
band strength in Table 1 was measured in a mixture with amorphous water ice at $T < 20$ K (Moore & Hudson 1998). Using this value in a pure amorphous ethanol ice introduces a similar uncertainty than that mentioned above.

A Pfeiffer Prisma quadrupole mass spectrometer (QMS) of a mass spectral range from 1 to 200 amu with a Channeltron detector was used to detect molecules in the gas phase. The QMS ionizes gas-phase molecules with ~ 70 eV electron bombardment, leading to fragmentation of the molecules with a given pattern. The species potentially desorbing into the phase were preferably monitored through their main mass fragment, which does not always coincide with the molecular ion. In some cases the main mass fragment of a given species was common to a mass fragment of another species (see, for example, Figs. 1 and 2 for the mass spectrum of ethanol and methanol, respectively, in our setup). When possible, alternative mass fragments were used in those cases (see Table 2). Fragments in Table 2 were also used in the experiments with the isotopically labeled molecules, but mass fragments with ^{13}C were 1 amu higher. There were two exceptions: $^{13}\text{CH}_4$ was monitored through the mass fragment $m/z = 15$, which corresponds to the $^{13}\text{CH}_2^+$ fragment, and $^{13}\text{CH}_3\text{OH}$ was monitored through the mass fragment $m/z = 33$, which corresponds to the molecular ion.

The targeted molecules of this work were CH_3OH and H_2CO . Methanol was monitored through its main mass fragment, $m/z = 31$. However, in the irradiation experiments of

Table 2. Mass fragments used to monitor potentially desorbing species into the gas phase.

Molecule	Molecular ion	Main mass fragment	Mass fragment used	Notes
C ₂ H ₅ OH	45	31	45	$m/z = 31$ was common to CH ₃ OH
H ₂ O	18	18	18	
CH ₄	16	16	15	$m/z = 16$ was common to H ₂ O
CH ₃ OH	32	31	31	Contribution from CH ₃ OH molecules was negligible CH ₃ OH could not be unambiguously detected in the gas phase during C ₂ H ₅ OH irradiation (see text)
H ₂ CO	30	29	29	$m/z = 30$ was also used (see text)
CH ₃ CHO	44	29	43	$m/z = 29$ was common to H ₂ CO $m/z = 44$ was common to CO ₂ CH ₃ CHO was not detected in the gas phase during irradiation in both series of experiments
C ₂ H ₆	30	28	27	$m/z = 28$ was common to CO $m/z = 30$ was common to H ₂ CO
CO	28	28	28	Contribution from other species was negligible
CO ₂	44	44	44	CO ₂ was not detected in the gas phase during irradiation in both series of experiments

**Fig. 2.** Mass spectrum of methanol in our setup.

pure C₂H₅OH ice, $m/z = 31$ was common to the main mass fragment of the ethanol molecules. The rest of mass fragments with a reasonable abundance, according to Fig. 2 ($m/z = 29$, $m/z = 32$, $m/z = 15$, $m/z = 28$, and $m/z = 30$), were also common to H₂CO, O₂, CH₄, CO, and H₂CO molecules, respectively. Therefore, CH₃OH could not be unambiguously detected in the gas phase in that series of experiments. The main mass fragment of H₂CO is $m/z = 29$, which was common to ethanol, methanol, and ethane (see below). Ethanol molecules could contribute in the first series of experiments with up to a 20% of the total $m/z = 29$ signal, according to the mass spectrum of this molecule in Fig. 2, since the level of the $m/z = 31$ signal (likely coming from ethanol, as explained below) was found to be comparable to the $m/z = 29$ mass fragment. Contribution from methanol molecules during the first series of experiments was not likely, since the behavior of the $m/z = 31$ signal follows that of the $m/z = 45$ signal, and it was therefore coming from ethanol molecules. Methanol was not detected in the gas phase in the second series of experiments. Contribution from ethane molecules could not be completely discarded during the first series of experiments, though. Although the second most abundant

fragment ($m/z = 30$) was used to double-check the detection formaldehyde molecules in the gas phase, contribution of ethane molecules to this fragment could not be discarded either in the first series of experiments.

Calibration of our QMS allows conversion from integrated ion currents into photon-induced desorbed column densities, using the equation

$$N(\text{mol}) = \frac{A(m/z)}{k_{\text{CO}}} \cdot \frac{\sigma^+(\text{CO})}{\sigma^+(\text{mol})} \cdot \frac{I_F(\text{CO}^+)}{I_F(z)} \cdot \frac{F_F(28)}{F_F(m)} \cdot \frac{S(28)}{S(m/z)}, \quad (2)$$

where $N(\text{mol})$ is the total number of photon-induced desorbed molecules cm^{-2} , $A(m/z)$ the integrated area below the QMS signal of a given mass fragment m/z during photon-induced desorption, k_{CO} is the proportionality constant between the integrated ion current and the column density of desorbed molecules in the case of a pure CO ice, as shown by

$$k_{\text{CO}} = \frac{A(28)}{N(\text{CO})} = k_{\text{QMS}} \cdot \sigma^+(\text{CO}) \cdot I_F(\text{CO}^+) \cdot F_F(28) \cdot S(28), \quad (3)$$

with k_{QMS} the proportionality constant independent of the species. The constant k_{CO} is regularly calculated with pure CO ice irradiation experiments. Parameter $\sigma^+(\text{mol})$ is the ionization cross section for the first ionization of the species of interest and the incident electron energy of the mass spectrometer; $I_F(z)$ is the ionization factor, that is, the fraction of ionized molecules with charge z ; $F_F(m)$ the fragmentation factor, that is, the fraction of molecules of the isotopolog of interest leading to a fragment of mass m in the mass spectrometer; and $S(m/z)$ the sensitivity of the QMS to the mass fragment (m/z). In practice, we work with the product $k_{\text{QMS}}^* \cdot S(m/z)$ (k_{QMS}^* indicates that pressure units are used instead of column density units), since the ratio $S(m/z)/S(28)$ is the same as the ratio $k_{\text{QMS}}^* \cdot S(m/z)/k_{\text{QMS}}^* \cdot S(28)$. Sensitivity of the QMS is also probed regularly, using noble gases. Calibration of the QMS is detailed in Martín-Doménech et al. (2015).

Equations (2) and (3) assume that the pumping speed in the ISAC setup is the same for all molecules, so that k_{QMS} does not depend on the species (see Martín-Doménech et al. 2015). In fact, the pumping speed depends on the molecular mass and, to a lesser extent, on the molecular structure (Kaiser et al. 1995). Constant k_{QMS} in Eq. (3) thus corresponds to the pumping speed of CO molecules. Therefore, $N(\text{mol})$ calculated with Eq. (2) is

Table 3. UV photoprocessing experiments of pure C₂H₅OH ices.

Experiment	$N_{\text{initial}}(\text{C}_2\text{H}_5\text{OH})$ $\times 10^{15}$ molecules cm^{-2}	Fluence $\times 10^{17}$ photons cm^{-2}	$N_{\text{final}}(\text{C}_2\text{H}_5\text{OH})$ $\times 10^{15}$ molecules cm^{-2}	$N_{\text{final}}(\text{CH}_3\text{OH})$ $\times 10^{15}$ molecules cm^{-2}	$N_{\text{final}}(\text{H}_2\text{CO})^a$ $\times 10^{15}$ molecules cm^{-2}
1	204.7	7.2	39.8	0.0	≤ 90.1
2	185.6	7.2	38.3	0.0	≤ 85.5

Notes. ^(a) This is an upper limit since the H₂CO IR band used is blended with two more bands corresponding to acetaldehyde and water.

only valid if the pumping speed of a specific species is the same as for CO. Taking the different pumping speeds into account, the real number of photon-induced desorbed molecules would be

$$N^{\text{real}}(\text{mol}) = N^{\text{calc}}(\text{mol}) \cdot S_{\text{rel}}(\text{mol}), \quad (4)$$

with $N^{\text{calc}}(\text{mol})$ the column density calculated with Eq. (2), and $S_{\text{rel}}(\text{mol})$ the relative pumping speed with respect to the CO molecules. According to the manufacturer of the pumping devices used in the ISAC setup, the relative pumping speed with respect to CO of a species with molecular mass $M(\text{mol})$ is

$$S_{\text{rel}}(\text{mol}) = 1.258 - 9.2 \times 10^{-3} \cdot M(\text{mol}). \quad (5)$$

Photon-induced desorption yields can be subsequently calculated by dividing $N^{\text{real}}(\text{mol})$ by the fluence (the product of the VUV-flux and the irradiation time).

A small rise in the signal of several mass fragments was detected every time the UV lamp was switched on. This effect has been previously reported in other works (see, e.g., Loeffler et al. 2005), but it was not reproducible so was difficult to quantify. When comparable to the rise produced by photon-induced desorption of molecules from the ice during the first series of experiments, calculated desorption yields were considered upper limits.

At the end of the experimental simulations, ice samples were warmed up to room temperature using a LakeShore Model 331 temperature controller, until a complete sublimation was attained. A silicon diode temperature sensor located close to the ice substrate was used, reaching a sensitivity of about 0.1 K. The IR spectra of the solid sample were collected every five minutes during warm-up. At the same time, all the desorbing species, including the components of the ice analogs and the products of the photochemical reactions, were detected by the QMS mentioned above.

3. Experimental results and discussion

3.1. UV photoprocessing of a pure C₂H₅OH ice

Table 3 presents the two experiments performed involving UV photoprocessing of a pure C₂H₅OH ice. The production of new species due to the energetic processing of the ice samples is studied in Sect. 3.1.1 by means of IR spectroscopy and mass spectrometry (during temperature-programmed desorption (TPD) of the ice sample at the end of the experiment). Photon-induced desorption of the photoproducts is studied in Sect. 3.1.2 by means of mass spectrometry.

3.1.1. Photon-induced chemistry of pure C₂H₅OH ice

An IR spectrum of the ice sample was collected after every irradiation interval to monitor the ice composition in the two experiments. Figure 3 shows the evolution of the mid-IR spectrum (between 3800 cm^{-1} and 750 cm^{-1}) of the ice sample in experiment 2. Similar results were found during experiment 1.

The IR spectrum of the ice sample is dominated by the C₂H₅OH features between 3600 cm^{-1} and 2650 cm^{-1} (Fig. 3a), 1580 cm^{-1} and 1230 cm^{-1} (Fig. 3c), and 1120 cm^{-1} and 860 cm^{-1} (Fig. 3d). New IR features appearing as the result of the UV photoprocessing of the ice samples were assigned to the formation of photoproducts. These assignments could be subsequently confirmed by monitoring the corresponding mass fragment during the TPD carried out at the end of the experiments. Figure 4 shows TPD spectra of selected mass fragments at the end of experiment 2. Results were similar during experiment 1.

The C₂H₅OH column density was best monitored with the IR band peaking at 1048 cm^{-1} shown in Fig. 3d. The intensity of this band gradually decreases with continuing irradiation, and $\sim 80\%$ of the initial ethanol was either photodissociated or, to a lesser extent, photodesorbed after a total fluence of 7.2×10^{17} photons cm^{-2} in the two experiments (see Table 3). A similar behavior is seen for the other C₂H₅OH features in Figs. 3a–d.

Photodissociation of C₂H₅OH triggered a complex photochemical network whose complete study is beyond the scope of this work. No evidence of CH₃OH formation was found during irradiation of the ice samples. In particular, the C–O stretching mode of CH₃OH that should appear at ~ 1016 cm^{-1} in a relatively clean region of the spectrum is not detected in Fig. 3d. Formation of CH₃OH in an extent below the sensitivity limit of our FTIR spectrometer is rejected since no desorption peak is detected with the more sensitive QMS for the $m/z = 31$ mass fragment at the desorption temperature of methanol (~ 145 K according to Martín-Doménech et al. 2014, see Fig. 4c). On the other hand, a new IR band is clearly detected at 1715 cm^{-1} in Fig. 3c, due to the C=O stretching mode of a carbonyl group, reaching its maximum intensity after 31 minutes of irradiation. Both H₂CO and CH₃CHO contribute to this band, since desorption peaks at ~ 121 K and ~ 116 K were detected for the mass fragments $m/z = 30$ (Fig. 4b) and $m/z = 43$ (Fig. 4d), respectively, confirming the presence of these species in the processed ice (desorption temperatures of pure H₂CO and CH₃CHO ices are ~ 112 K and ~ 105 K, respectively, according to Noble et al. 2012; Öberg et al. 2009). An upper limit to the column density of H₂CO in the ice is shown in Table 3. Up to 45% of the initial ethanol was converted into formaldehyde at the end of the experiments.

A broad band on the red side of the C=O stretching mode of carbonyl groups is due to blending with the water O–H bending mode. Other four carbon-bearing species were formed during UV photoprocessing of the pure ethanol ice. The C–H stretching and the deformation modes of CH₄ are clearly detected at 3005 cm^{-1} and 1302 cm^{-1} after 15 min of irradiation (see Figs. 3a and c, respectively). The deformation mode of C₂H₆ is also detected at 1349 cm^{-1} (Fig. 3c) after six minutes of irradiation. The presence of ethane in the ice sample was confirmed during the TPD at the end of the experiments (see Fig. 4a). Finally, the C–O stretching band of CO is clearly detected at

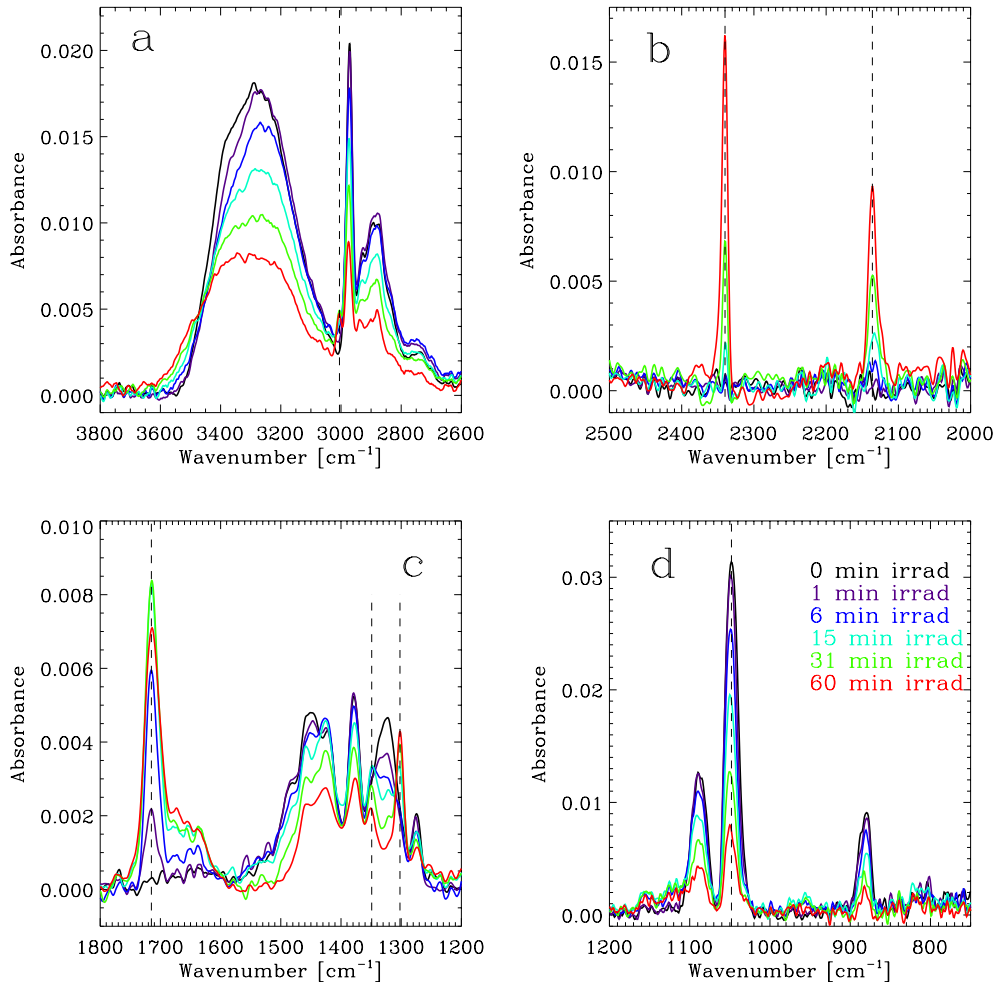


Fig. 3. Evolution of the IR spectrum of the ice sample during UV photoprocessing in experiment 2 (see Table 3) conveniently split in four regions. Results were similar in experiment 1. **a)** A new feature appears at 3005 cm^{-1} (dashed line) between the O-H and C-H stretching bands of $\text{C}_2\text{H}_5\text{OH}$, which is attributed to the formation of CH_4 . This species also displays a more intense band near 1302 cm^{-1} , shown in panel **c)**. **b)** Formation of CO_2 and CO leads to the appearance of two C-O stretching bands at 2340 cm^{-1} and 2136 cm^{-1} (dashed lines), respectively. **c)** Dashed lines at 1715 cm^{-1} , 1349 cm^{-1} , and 1302 cm^{-1} indicate new features due to the formation of photoproducts (probably H_2CO , CH_3CHO , C_2H_6 , and CH_4 ; see text). A broad band on the red side of the 1715 cm^{-1} peak may indicate the presence of H_2O . **d)** Intensity of the C-O stretching band of $\text{C}_2\text{H}_5\text{OH}$ at 1048 cm^{-1} (dashed line) decreases as the ice is processed.

2136 cm^{-1} , while the C-O stretching band of CO_2 molecules is observed at 2340 cm^{-1} (Fig. 3b).

3.1.2. Photon-induced desorption from pure $\text{C}_2\text{H}_5\text{OH}$ ice

A QMS was used during UV photoprocessing of the ice samples to monitor the photon-induced desorption of the photoproducts detected in Sect. 3.1.1 using the mass fragments selected in Sect. 2. Results are shown in Fig. 5.

Photon-induced desorbing species presented a rise in the QMS ion current of their corresponding mass fragments during irradiation. As mentioned in Sect. 2, calibration of the QMS allowed us to obtain desorption yields of the photon-induced desorbing species from the integrated ion currents. Parameters used in Eq. (2) for the photoproducts in experiments 1 and 2 are shown in Table 4. Proportionality constant k_{CO} was $1.74 \times 10^{-10}\text{ A min ML}^{-1}$ for both experiments. Photon-induced desorption yields of all photoproducts in pure ethanol ice irradiation experiments (except for CH_3CHO and CO_2 , whose desorption, if taking place, was negligible) are presented in Table 5 for experiment 2, averaged for each irradiation period. Results were similar in experiment 1.

Evolution of the photodesorption yield with fluence is related to the two main photon-induced desorption mechanisms presented in Sect. 1. Photoproducts that are able to desorb through the process called indirect desorption induced by electronic transitions (DIET) increase their photodesorption yield (or in other words, their QMS ion current during irradiation) with fluence, since molecules previously formed and accumulated in the bulk of the ice are later available for desorption when a photon is absorbed by a nearby molecule (indirect DIET photodesorption is also included). On the other hand, photochemidesorbing-only species do not increase their photodesorption yield (or ion current) with fluence, since only molecules formed on the surface of the ice are able to desorb right after their formation, and molecules accumulated in the bulk of the ice are not able to desorb later on during irradiation. In the case of molecules able to both photochemidesorb and desorb through the DIET mechanisms, the effect of the former will be negligible compared to the latter since the number of molecules at the surface of the ice is much lower than in the bulk (see also Fillion et al. 2014).

Photon-induced desorption of methanol was discarded since the behavior of the $m/z = 31$ signal follows that of the

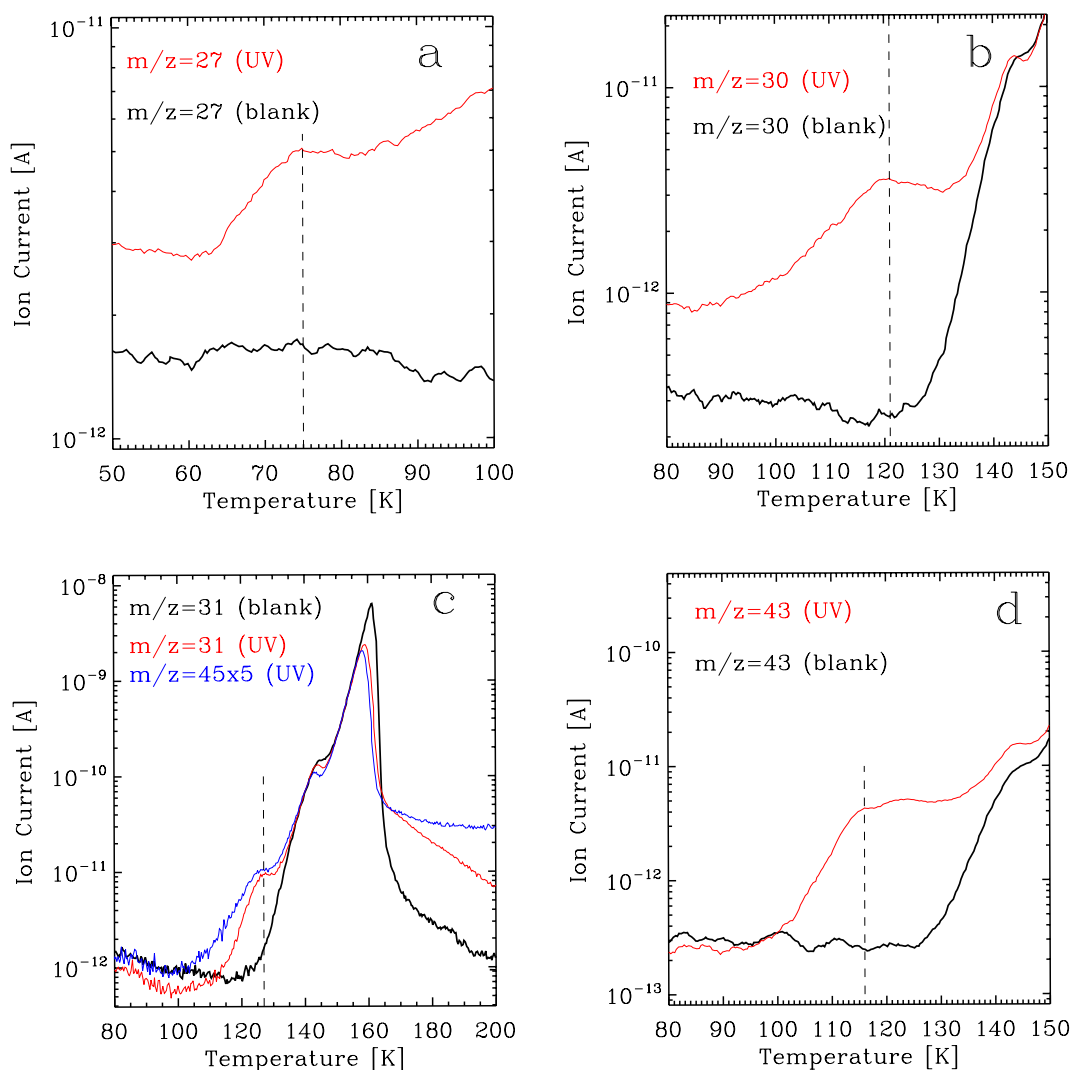


Fig. 4. TPD curves displaying the thermal desorption of photoproducts through selected mass fragments at the end of experiment 2 (see Table 3) in red, compared to the blank experiment with no irradiation (black). **a)** TPD curves of the $m/z = 27$ mass fragment, corresponding to the $C_2H_3^+$ fragment of C_2H_6 . A desorption peak at ~ 75 K (dashed line) confirms the presence of ethane in the processed ethanol ice (desorption of a pure ethane ice takes place above 60 K according to Öberg et al. 2009). **b)** TPD curves of the $m/z = 30$ mass fragment, corresponding to the molecular ion of H_2CO . The desorption peaking at ~ 121 K (dashed line) confirms the formation of formaldehyde during UV photoprocessing of a pure ethanol ice (see text). **c)** TPD curves of the $m/z = 31$ mass fragment corresponding to the CH_3O^+ fragment of CH_3OH . Since no excess in the desorption is detected at ~ 145 K compared to the blank, formation of methanol during UV photoprocessing of a pure ethanol ice is negligible. Desorption at ~ 127 K (dashed line) is probably due to an earlier ethanol desorption triggered by less polar and more volatile components in the ice matrix that were not present in the blank experiment (mainly formaldehyde and acetaldehyde), since it is shared with the $m/z = 45$ mass fragment (blue). **d)** TPD curves of the $m/z = 43$ mass fragment, corresponding to the CH_3CO^+ fragment of CH_3CHO . The desorption peaking at ~ 116 K (dashed line) confirms the formation of acetaldehyde during UV photoprocessing of a pure ethanol ice (see text).

$m/z = 45$ signal, and it was therefore coming from ethanol molecules. On the other hand, ion currents of mass fragments $m/z = 29$ and $m/z = 30$ in Fig. 5a present rather constant rises during UV irradiation of the ice sample, suggesting photochemidesorption. As explained in Sect. 2, either formaldehyde and/or ethane molecules could be responsible for the detected mass fragments, since a similar rise is detected for the ethane mass fragment $m/z = 27$ in Fig. 5b. This means that one out of two, or even both species could be photochemidesorbing to the gas phase during irradiation of the pure ethanol ice. Therefore, we used the integrated ion currents of mass fragment $m/z = 30$ and the parameters shown in Table 4 for both species to extract upper limits to their photon-induced desorption yields (see Table 5). The average photon-induced desorption yield would be of $\sim 6.2 \times 10^{-5} \frac{\text{molecules}}{\text{incident photon}}$ if the $m/z = 30$ signal was due only to

formaldehyde molecules, and of $\sim 1.1 \times 10^{-4} \frac{\text{molecules}}{\text{incident photon}}$ if only ethane molecules contributed to the signal. These values should be considered upper limits due to the possible contribution from the small rise experienced by the ion current when the UV lamp was switched on during this series of experiments (see Sect. 2). In both cases the photon-induced desorption yields remain almost constant with fluence, as expected for photochemidesorbing species.

Figure 5b shows the evolution during photoprocessing of a pure ethanol ice for the mass fragments corresponding to other photoproducts detected in Sect. 3.1.1. Apart from the $m/z = 27$ mass fragment corresponding to ethane molecules commented above, the ion current of mass fragments $m/z = 15$ (CH_3^+), $m/z = 18$ (H_2O^+), and $m/z = 28$ (CO^+) were found to increase from one irradiation interval to the next, indicating

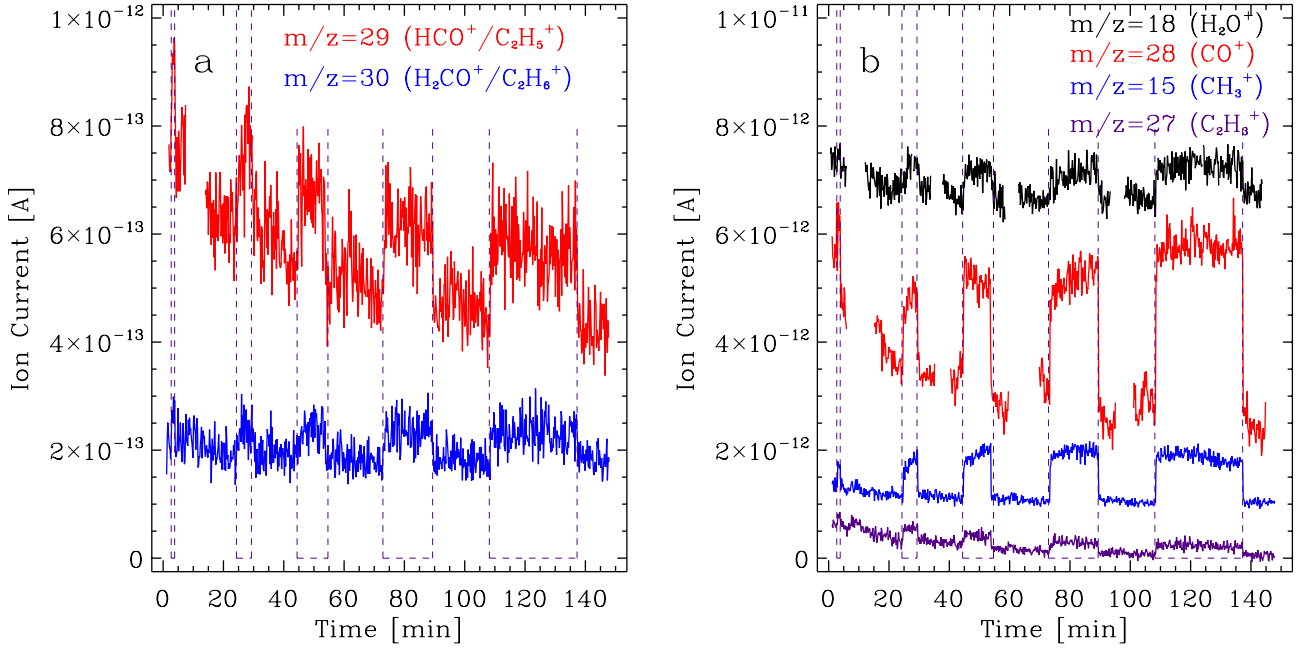


Fig. 5. Photon-induced desorption of several photoproducts during irradiation of a pure ethanol ice in experiment 2, see Table 3. Results were similar in experiment 1. Irradiation intervals are indicated with vertical dashed lines. Signal due to rotation of the sample holder between irradiation intervals were omitted. **a)** Photochemidesorption of formaldehyde/ethane (see text) observed with mass fragments $m/z = 29$ and $m/z = 30$. **b)** Photochemidesorption of water and ethane observed with mass fragments $m/z = 18$ and $m/z = 27$, respectively. DIET photodesorption was detected for CO and CH₄ ($m/z = 28$ and $m/z = 15$, respectively). Ion currents of different mass fragments are offset for clarity.

Table 4. Values used in Eq. (2) to convert integrated QMS signals for the mass fragments into column densities of desorbing molecules.

Factor	H ₂ CO	C ₂ H ₆	H ₂ O	CH ₄	CO
σ^+ (mol) (\AA^2) ^a	4.140	6.422	2.275	3.524	2.516
fragment	H ₂ CO ⁺	C ₂ H ₆ ⁺	H ₂ O ⁺	CH ₃ ⁺	CO ⁺
m/z	30	30	18	15	28
$I_F(z)$	1 ^b	1 ^b	1 ^b	1 ^b	1 ^b
$F_F(m)$	0.319 ^a	0.121 ^c	0.806 ^c	0.406 ^c	0.949 ^c
$k_{\text{QMS}}^* \cdot S(m/z)$ (A mbar ⁻¹ \AA^{-2}) ^d	1.77×10^{15}	1.77×10^{15}	3.86×10^{15}	4.69×10^{15}	2.02×10^{15}
$k_{\text{QMS}}^* \cdot S(m/z)$ (A mbar ⁻¹ \AA^{-2}) ^e	9.30×10^{14}	9.30×10^{14}	1.69×10^{15}	1.97×10^{15}	1.03×10^{15}
$k_{\text{QMS}}^* \cdot S(m/z)$ (A mbar ⁻¹ \AA^{-2}) ^f	1.29×10^{15}	1.29×10^{15}	2.50×10^{15}	2.94×10^{15}	1.44×10^{15}
S_{rel} (mol) ^g	0.982	0.982	1.092	1.111	1.000

Notes. ^(a) Extracted from the online database of the National Institute of Standard and Technologies (NIST); ^(b) a value of 1 was adopted, assuming that no double ionization of the molecules takes place; ^(c) extracted from the mass spectral library of the QMS software; ^(d) calculated for our QMS and valid for experiments 1, 2, 6, 9, and 10 (see Sect. 2); ^(e) for experiments 3 and 7 (see Sect. 2); ^(f) for experiments 4, 5, and 8 (see Sect. 2); ^(g) calculated with Eq. (4).

that the photoproducted methane, water, and carbon monoxide, respectively, are able to desorb through the DIET mechanism during irradiation of a pure ethanol ice. In the case of CH₄, this behavior is different from the one experienced by the molecules photoproducted in a pure methanol ice, which were able to photochemidesorb but not to desorb through the DIET mechanism (Cruz-Díaz et al., in prep.).

In pure methane ice, CH₄ molecules are not able to desorb, probably because methane molecules are readily photodissociated by the VUV photons, and they cannot trigger the DIET photodesorption mechanism. Therefore, in a methanol or ethanol ice, the DIET photodesorption process of methane molecules would be triggered more likely by the absorption of the VUV photons by molecules of other species in the subsurface layers of the ice (indirect DIET). The different behavior in these two ice

irradiation experiments indicates that the energy redistributed to methane molecules in the surface of the ice is enough to break the intermolecular bonds in the case of pure ethanol ice irradiation experiments, but not during irradiation of a pure methanol ice. This may be due to a higher intermolecular binding energy of methane molecules to their neighbors in the methanol ice irradiation experiments or, alternatively, to a higher energy redistributed by the absorbing molecules to the surface in the ethanol ice experiments.

The photodesorption yield of water and methane molecules reached a constant value after approximately 15 min of irradiation, of $\leq 2.6 \times 10^{-4} \frac{\text{molecules}}{\text{incident photon}}$, and $\sim 3.3 \times 10^{-4} \frac{\text{molecules}}{\text{incident photon}}$, respectively (see Table 5). The photodesorption yield of CO molecules increased with fluence (Table 5) during the full experiment.

Table 5. Evolution of the photon-induced desorption yields during UV irradiation of a pure C₂H₅OH ice.

Irradiation period (min)	Fluence ^a (photons cm ⁻²)	$Y_{\text{pd}}(\text{H}_2\text{CO})^{b,c}$	$Y_{\text{pd}}(\text{C}_2\text{H}_6)^{b,c}$	$Y_{\text{pd}}(\text{H}_2\text{O})^{b,c}$	$Y_{\text{pd}}(\text{CH}_4)^b$	$Y_{\text{pd}}(\text{CO})^b$
		$10^{-5} \left(\frac{\text{molecules}}{\text{incident photon}} \right)$		$10^{-4} \left(\frac{\text{molecules}}{\text{incident photon}} \right)$		$10^{-3} \left(\frac{\text{molecules}}{\text{incident photon}} \right)$
0–1	1.2×10^{16}	≤ 7.6	≤ 1.3	≤ 1.1	1.8	0.6
1–6	7.2×10^{16}	≤ 5.9	≤ 1.0	≤ 2.0	2.3	0.7
6–15	1.8×10^{17}	≤ 5.5	≤ 1.0	≤ 2.7	3.1	1.0
15–31	3.7×10^{17}	≤ 6.4	≤ 1.1	≤ 2.4	3.4	1.1
31–60	7.2×10^{17}	≤ 5.8	≤ 1.0	≤ 2.7	3.2	1.5

Notes. ^(a) Total fluence at the end of the irradiation period; ^(b) averaged for each irradiation period in experiment 2. Results were similar in experiment 1. Photon-induced desorption yield values could be different by a factor 2 due to the uncertainties in all the parameters of Eq. (2); ^(c) we consider these values upper limits due to possible contribution from other species to the signal of the selected mass fragment and/or from the small rise experienced by the ion currents when the UV lamp is switched on (see Sect. 2).

Table 6. UV photoprocessing experiments of H₂O:CH₄ ice analogs.

Experiment	$N_{\text{initial}}(\text{H}_2\text{O})$	$N_{\text{initial}}(\text{CH}_4)$	Fluence $\times 10^{17}$ photons cm ⁻²	$N_{\text{final}}(\text{H}_2\text{O})$	$N_{\text{final}}(\text{CH}_4)$	$N_{\text{final}}(\text{CH}_3\text{OH})$	$N_{\text{final}}(\text{H}_2\text{CO})^a$
	$\times 10^{15}$ molecules	cm ⁻²		$\times 10^{15}$ molecules	cm ⁻²	cm ⁻²	
3	426.7	119.2	7.2	376.0	62.0	7.2	...
4	586.2	229.6	7.8	520.9	173.8	7.8	...
5	898.2	216.3	10.8	878.2	153.7	4.9	...
6	560.1	161.3	7.2	500.1	101.2	4.2	...
7 ^b	506.6	150.6	7.2	462.4	89.0	0.0	...
8 ^b	721.9	263.0	10.8	665.4	165.3	0.4	...
9 ^b	372.9	160.2	7.2	335.0	90.6	1.8	...
10 ^b	523.7	146.8	6.0	... ^c	... ^c	... ^c	... ^c

Notes. ^(a) Formaldehyde was barely detected by means of IR spectroscopy, and no quantification was possible. Formation of H₂CO was confirmed during the TPD. ^(b) ¹³CH₄ was used instead of CH₄ in these experiments. ^(c) No IR spectrum was collected at the end of this experiment, since it focused only on measuring QMS signals during irradiation (see Fig. 10).

3.2. UV photoprocessing of a H₂O:CH₄ ice analog

The second series of experiments involved the UV photoprocessing of a more realistic, water-rich ice analog. A binary H₂O:CH₄ ice analog was used in experiments 3 to 10 described in Table 6. The initial ice composition in this series of experiments was held, approximately, to 75% of water and 25% of methane. The irradiation time changed from one experiment to the next so that the total fluence was, approximately, one photon per initial molecule. In experiments 7–10 we used ¹³CH₄ instead of CH₄ to confirm the results found in experiments 3–6 and to reject fake positives due to contamination. As in Sect. 3.1, we used the FTIR spectrometer to monitor the ice composition after every irradiation interval and to detect new IR features corresponding to the formation of photoproducts. The presence of these new species could be subsequently confirmed during the TPD performed at the end of the experiments when necessary. Results for the photon-induced chemistry are shown in Sect. 3.2.1. At the same time, the QMS was used during irradiation to detect the molecules desorbing into the gas phase as a consequence of the UV photoprocessing. Photon-induced desorption is studied in Sect. 3.2.2.

3.2.1. Photon-induced chemistry of a H₂O:CH₄ ice analog

Figure 6 shows the evolution of the mid-IR spectrum of the ice sample in experiment 6 between 4400 cm⁻¹ and 910 cm⁻¹,

and Fig. 7 shows the mid-IR spectra between 2500 cm⁻¹ and 910 cm⁻¹ of the ice sample in experiment 9. Results were similar for the rest of the experiments. As expected, some of the IR features are shifted in the experiments with ¹³CH₄. In particular, the C-H deformation band of CH₄ shifts from 1300 cm⁻¹ in Fig. 6d to 1292 cm⁻¹ in Fig. 7c. Bands of C-bearing photoproducts are also shifted in a similar way (see below).

The initial components of the ice analogs were monitored with the O-H stretching band at ~ 3280 cm⁻¹ corresponding to water molecules (Fig. 6a), and in the C-H deformation band mentioned above corresponding to methane (Figs. 6d and 7c). The intensity of these bands gradually decrease with continuing irradiation, leading to a loss of $\sim 11\%$ of initial H₂O and $\sim 35\%$ of initial CH₄ molecules at the end of experiments 3–6 (Table 6). Loss of water was similar within 10% in experiments with ¹³CH₄, while loss of methane was about 40% higher, with no obvious explanation.

In this series of experiments, formation of CH₃OH during UV photoprocessing of the ice analogs was observed, thanks to the detection of the C-O stretching band at 1016 cm⁻¹ in Fig. 6d and at 1000 cm⁻¹ in Fig. 7c. The column density of methanol in the ice at the end of irradiation in experiments 3–6 accounts for $\sim 4\%$ of the initial CH₄ column density (Table 6). Formation of methanol took place to a lower extent in experiments 7–10. It did not reach the sensitivity limit of our FTIR in experiment 7 (see Table 6), but it was detected by the QMS during TPD (not shown). On the other hand, the relatively strong O-H bending

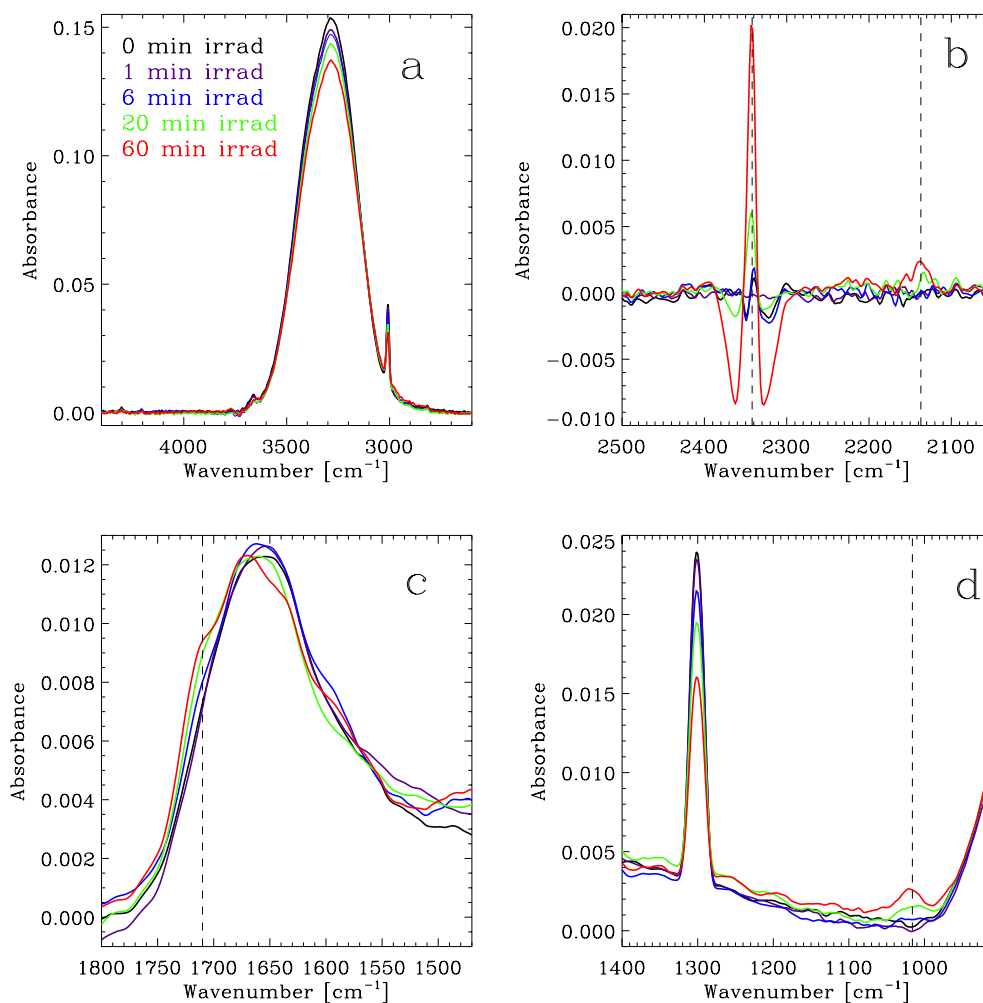


Fig. 6. Evolution of the IR spectrum of the $\text{H}_2\text{O}:\text{CH}_4$ ice mixture during UV photoprocessing in experiment 6, see Table 6. Results were similar in experiments 3–5. **a)** Evolution of the O-H stretching band of H_2O (broad band peaking at $\sim 3280\text{ cm}^{-1}$), and the C-H stretching band of CH_4 (in the red side of the former). **b)** Formation of CO_2 and CO leads to the appearance of two C-O stretching bands at 2342 cm^{-1} and 2137 cm^{-1} , respectively (dashed lines). Negative absorbances are due to the atmospheric correction applied by the FTIR software, but the band is due to solid CO_2 , as the peak position indicates. **c)** Evolution of the O-H deformation band of H_2O . The appearance of a shoulder at $\sim 1710\text{ cm}^{-1}$ is probably due to the formation of H_2CO . **d)** Evolution of the C-H deformation band of CH_4 at 1300 cm^{-1} . The new feature at 1016 cm^{-1} is due to the formation of methanol.

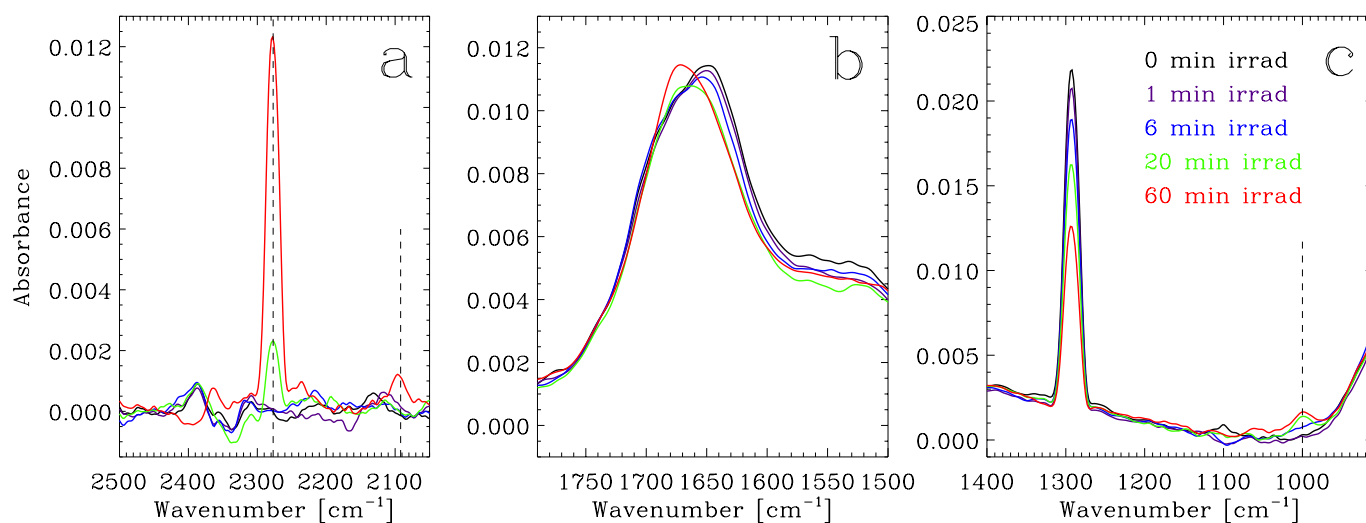


Fig. 7. Evolution of the IR spectrum of the $\text{H}_2\text{O}:\text{CH}_4$ ice mixture during UV photoprocessing in experiment 9, see Table 6. Results were similar in experiments 7, 8, and 10. **a)** Formation of $^{13}\text{CO}_2$ and ^{13}CO leads to the appearance of two C-O stretching bands at 2277 cm^{-1} and 2092 cm^{-1} , respectively (dashed lines). **b)** Evolution of the O-H deformation band of H_2O . **c)** Evolution of the C-H deformation band of CH_4 at 1292 cm^{-1} . The new feature at 1000 cm^{-1} is due to the formation of methanol.

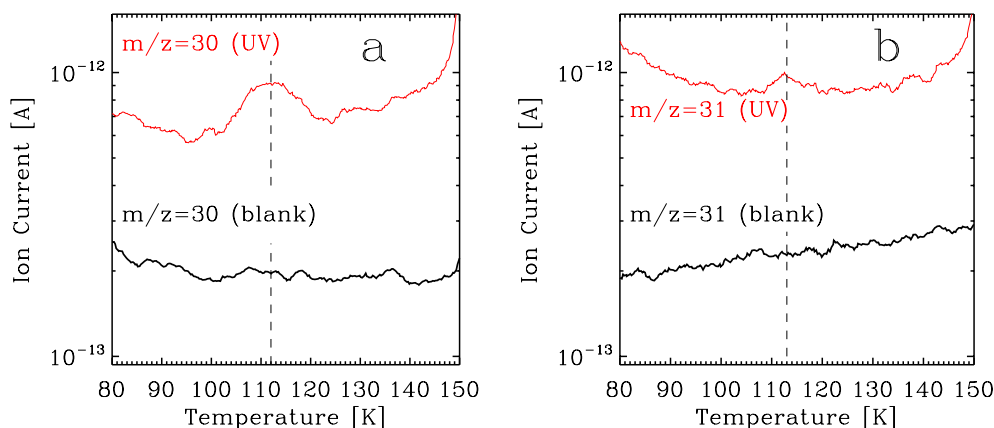


Fig. 8. **a)** TPD curve of the $m/z = 30$ mass fragment, corresponding to the molecular ion of H_2CO , after irradiation in experiment 3 (red) compared to the blank (black). A desorption peak at ~ 112 K (dashed line) confirms the formation of formaldehyde. **b)** TPD curve of the $m/z = 31$ mass fragment, corresponding to the molecular ion of H_2^{13}CO , after irradiation in experiment 7 (red) compared to the blank (black). A desorption peak at ~ 113 K (dashed line) confirms the formation of formaldehyde.

band that is due to water molecules prevented us from clearly detecting the C=O stretching mode of H_2CO in Figs. 6c and 7b. A shoulder at ~ 1715 cm^{-1} is observed on the blue side of the O-H bending band in Fig. 6c, while a shift in the peak frequency of this band is observed in Fig. 7b. Formation of H_2CO was confirmed during the TPD performed at the end of the experiments. A peak near the desorption temperature of pure H_2CO (~ 112 K, Noble et al. 2012) was observed for the mass fragments $m/z = 30$, corresponding to H_2CO^+ in experiments 3–6 (Fig. 8a), and $m/z = 31$, corresponding to $\text{H}_2^{13}\text{CO}^+$ in experiments 7–10 (Fig. 8b). However, photoproduction of formaldehyde could not be quantified using the IR spectra, since its IR band was barely detected.

Photochemistry was simpler in this series of experiments. In addition to CH_3OH and H_2CO , only CO and CO_2 were detected in the IR spectra. The C-O stretching mode of these molecules is observed at 2137 cm^{-1} and 2342 cm^{-1} , respectively, in Fig. 6b. The C-O stretching bands of ^{13}CO and $^{13}\text{CO}_2$ are redshifted to 2092 cm^{-1} and 2277 cm^{-1} in Fig. 7a, respectively, in fair agreement with the values reported in Gerakines et al. (1995).

3.2.2. Photon-induced desorption from a $\text{H}_2\text{O}:\text{CH}_4$ ice analog

As in Sect. 3.1.2, the QMS allowed us to detect desorption of the photoproducts observed in Sect. 3.2.1 during irradiation of the ice analogs, monitoring the mass ion fragments selected in Sect. 2. Results are shown in Figs. 9 and 10. As explained in Sect. 2, mass fragments in experiments 7–10 were 1 amu higher than in exp. 3–6 because of the presence of ^{13}C in the molecules. Photon-induced desorption yields were calculated for experiments 7–10 using the parameters shown in Table 7, since experiments with isotopically labeled molecules are more reliable thanks to the lack of contamination effects. Compared to the $m/z = 31$ fragment that corresponds to the molecular ion $\text{H}_2^{13}\text{CO}^+$, the H^{13}CO^+ fragment ($m/z = 30$) displayed a more intense signal with a lower noise level. Therefore, the latter was used to quantify the formaldehyde photon-induced desorption yield (the molecular ion was used in exp. 1–2). Proportionality constant k_{CO} varied between 1.35×10^{-10} A min ML^{-1} and 1.90×10^{-10} A min ML^{-1} for experiments 7–10. Table 8 shows the photon-induced desorption yields measured in experiment 9, averaged for every irradiation interval. Results were similar in experiments 7, 8, and 10.

Table 7. Values used in Eq. (2) to convert integrated QMS signals in experiments 7–10 (see Table 6) into column densities of desorbed molecules.

Factor	H_2^{13}CO	^{13}CO
σ^+ (mol) (\AA^2) ^a	4.140	2.516
Fragment	H^{13}CO^+	$^{13}\text{CO}^+$
m/z	30	29
$I_F(z)$	1 ^b	1 ^b
$F_F(m)$	0.549 ^c	0.949 ^d
$k_{\text{QMS}}^* \cdot S(m/z)$ (A mbar ⁻¹ \AA^{-2}) ^e	9.30×10^{14}	9.77×10^{14}
$k_{\text{QMS}}^* \cdot S(m/z)$ (A mbar ⁻¹ \AA^{-2}) ^f	1.29×10^{15}	1.36×10^{15}
$k_{\text{QMS}}^* \cdot S(m/z)$ (A mbar ⁻¹ \AA^{-2}) ^g	1.77×10^{15}	1.89×10^{15}
S_{rel} (mol) ^h	0.973	0.991

Notes. ^(a) We used the values corresponding to H_2^{12}CO and ^{12}CO , extracted from the online NIST database, as an approximation; ^(b) a value of 1 was adopted, assuming that no double ionization of the molecules takes place; ^(c) we used the value corresponding to the fragment H^{12}CO^+ , extracted from the online NIST database, as an approximation; ^(d) we used the value corresponding to the molecular ion $^{12}\text{CO}^+$, extracted from the mass spectra library of the QMS software, as an approximation; ^(e) calculated for our QMS and valid for experiment 7 (see Sect. 2); ^(f) for experiment 8 (see Sect. 2); ^(g) for experiment 9 and 10 (see Sect. 2); ^(h) calculated with Eq. (4).

No clear photon-induced desorption was observed for the mass fragments $m/z = 31$ (left panel of Fig. 9) and $m/z = 33$ (left panel of Fig. 10) corresponding to methanol molecules in experiments 3–6 and 7–10, respectively. On the other hand, a constant rise was detected during irradiation in experiments 3–6 for mass fragments $m/z = 29$ and $m/z = 30$ (left panel of Fig. 9), suggesting photochemidesorption of formaldehyde. The same behavior is observed in mass fragments $m/z = 30$ and $m/z = 31$ in experiments 7–10 (left panel of Fig. 10). This confirms photochemidesorption of formaldehyde, since the fragments of H_2^{13}CO are 1 amu higher than those of H_2CO . Averaged photodesorption yields of H_2^{13}CO in Table 8 are slightly lower than the upper limits derived in Sect. 3.1.2 for the pure $\text{C}_2\text{H}_5\text{OH}$ ice photoprocessing experiments.

Desorption of CO molecules during irradiation is detected in the righthand panel of Fig. 9 with the mass fragment $m/z = 28$. The DIET-like behavior of the photon-induced desorption is more clearly observed with the mass fragment $m/z = 29$ in the

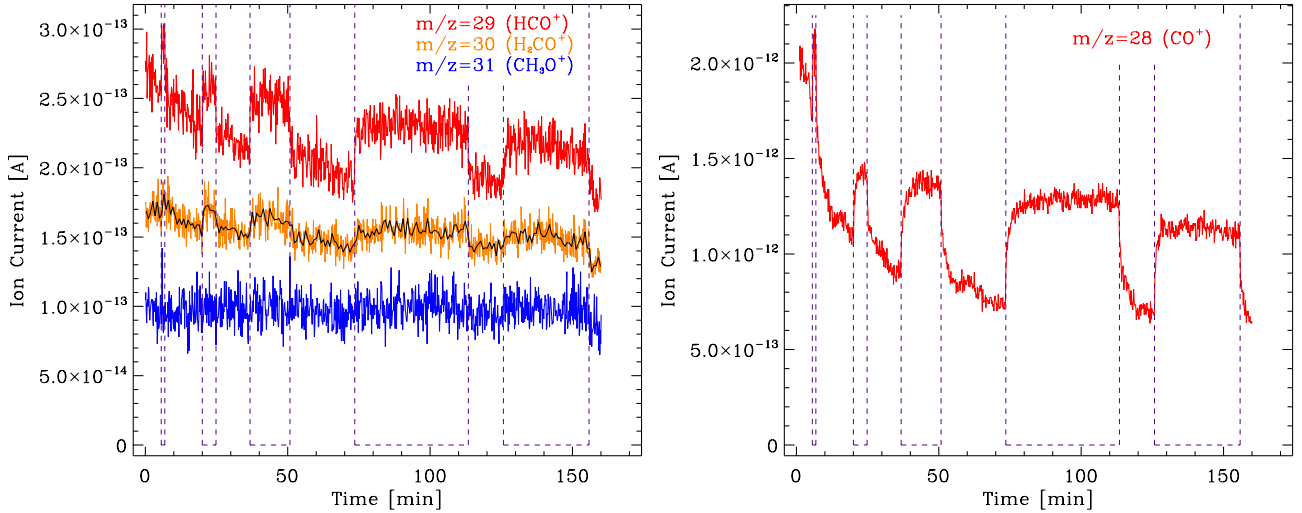


Fig. 9. Photon-induced desorption of formaldehyde observed with mass fragments $m/z = 29$ and $m/z = 30$ (left panel), and carbon monoxide ($m/z = 28$ in right panel) during UV irradiation of a $\text{H}_2\text{O}:\text{CH}_4$ ice analog in experiment 5. Results were similar in exp. 3, 4, and 6. Ion currents of different mass fragments are offset for clarity. The black solid line represent an average of the corresponding ion current, shown to better evaluate the shape of the signal. Irradiation intervals are indicated with dashed vertical lines.

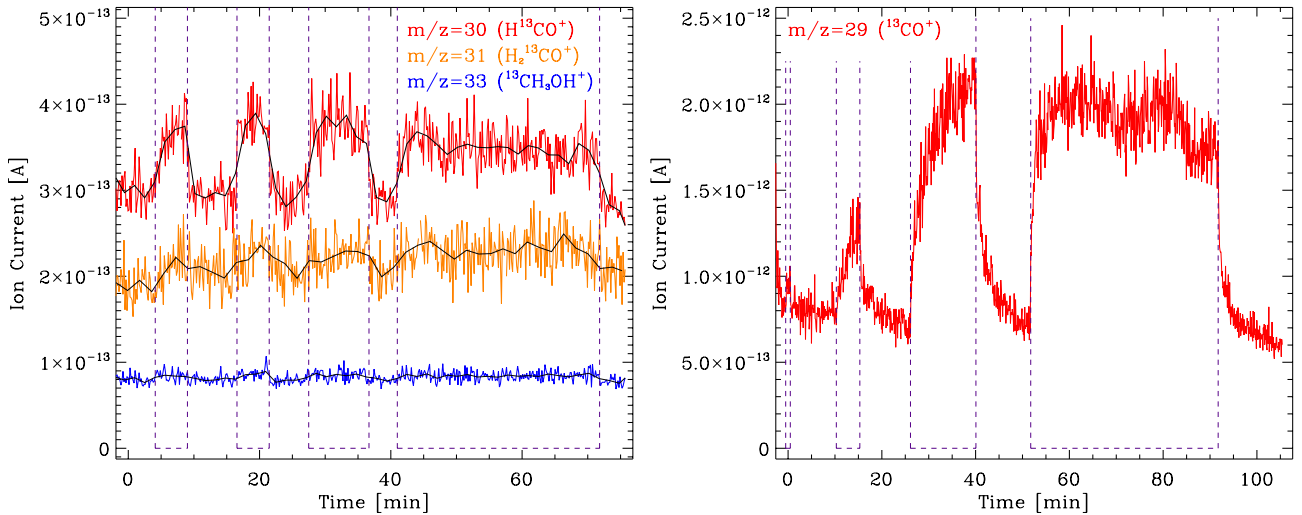


Fig. 10. Photon-induced desorption of H_2^{13}CO ($m/z = 30$ and $m/z = 31$ in left panel) and ^{13}CO ($m/z = 29$ in right panel) during UV irradiation of a $\text{H}_2\text{O}:\text{CH}_4$ ice analog in experiments 10 and 7, respectively. Results were similar for experiments 8 and 9. Ion currents of different mass fragments are offset for clarity. Black solid lines represent an average of the corresponding ion currents, shown to better evaluate the shape of the signals. Irradiation intervals are indicated with dashed vertical lines.

righthand panel of Fig. 10. The increasing photodesorption yield of ^{13}CO in Table 8 is one order of magnitude lower than that found in Sect. 3.1.2. This is probably due to the much lower formation rate found for the CO molecules in this series of experiments. After a fluence of $7.2 \text{ photons cm}^{-2}$, only $\sim 0.5\%$ of the initial column density had formed CO in experiments 3–10, while the value in experiments 1 and 2 is $\sim 13\%$ (see the low intensity of the C–O stretching band corresponding to CO in Figs. 6b and 7a compared to Fig. 3b). Photon-induced desorption of CO_2 was not observed in experiments 3–10 (not shown in Figs. 9 and 10).

4. Astrophysical implications

In cold dense interstellar and circumstellar regions, molecules form ice mantles upon freeze-out onto cold dust grains. These ice mantles are mainly observed in the near- to far-IR region

of the spectrum (Boogert et al. 2015, and references therein). Solid H_2O is the most abundant species observed in interstellar and circumstellar ices with an average abundance of $\sim 4 \times 10^{-5}$ relative to N_{H} (Boogert et al. 2015). Several other species have been confirmed to be present in ice mantles, in particular, CO, CO_2 , CH_3OH , NH_3 and CH_4 . Solid methane has been detected with abundances ranging from 0.4% to 11% relative to water ice (Boogert et al. 2015, and references therein). In the second series of experiments, we used binary $\text{H}_2\text{O}:\text{CH}_4$ ice analogs with a methane abundance that is somehow higher ($\sim 33\%$). More species have been tentatively identified in interstellar and circumstellar ices, some of them observed in comets. As mentioned in Sect. 1, $\text{C}_2\text{H}_5\text{OH}$ has been suggested as one of the possible carriers of the $7.24 \mu\text{m}$ IR band (Schutte et al. 1999). Schriver et al. (2007) derived an upper limit to the abundance of ethanol in interstellar ices of 1.2% relative to water ice from ISO observations. In addition, the presence of solid ethanol is needed to

Table 8. Evolution of the photodesorption yields during UV irradiation of a binary H₂O:¹³CH₄ ice analog in exp. 9, see Table 6.

Irradiation period (min)	Fluence ^a (photons cm ⁻²)	$Y_{\text{pd}}(\text{H}_2^{13}\text{CO})^b$ $10^{-5} \left(\frac{\text{molecules}}{\text{incident photon}} \right)$	$Y_{\text{pd}}(^{13}\text{CO})^b$ $10^{-4} \left(\frac{\text{molecules}}{\text{incident photon}} \right)$
0–1	1.2×10^{16}	4.3	0.8
1–6	7.2×10^{16}	3.9	0.9
6–20	2.4×10^{17}	4.8	1.5
20–60	7.2×10^{17}	4.4	4.9

Notes. Results were similar in experiments 7, 8, and 10. ^(a) Total fluence at the end of the irradiation period. ^(b) Averaged for each irradiation period in experiment 9. Photon-induced desorption yield values could be different by a factor 2 due to the uncertainties in all the parameters of Eq. (2).

explain gas-phase abundances in dense star-forming regions that cannot be reproduced by pure gas-phase chemical models. Pure ethanol ice samples were used for our first series of experiments.

Ice mantles can be energetically processed by cosmic rays, UV, and X-ray photons, and also thermally in regions around protostars. Energetic processing of ices leads to several effects, including photon-induced chemistry and photon-induced desorption as studied in this work. Solid-phase chemistry has been widely proposed as a possible source of molecules in the ISM. In some cases, formation in ice mantles followed by nonthermal desorption needs to be invoked to explain the observed abundances of some species in dense cores and low UV-field illuminated PDRs. This is the case of the targeted molecules of this work, CH₃OH and H₂CO (see Sect. 1). Photoprocessing in particular takes place in dense cores thanks to the secondary UV field generated by the interaction of H₂ molecules in the gas phase with cosmic rays, leading to a photon flux of $\sim 10^4$ photons cm⁻² s⁻¹ (Cecchi-Pestellini & Aiello 1992; Shen et al. 2004). On the other hand, PDRs are illuminated by nearby massive stars with a UV flux of $\sim 10^{11}$ eV cm⁻² s⁻¹ for a low UV-field illuminated PDR as for the Horsehead PDR (Pety et al. 2012). In our experiments, we used a MDHL with a photon flux of $\sim 2 \times 10^{14}$ photons cm⁻² s⁻¹ and an average photon energy of 8.6 eV (see Sect. 2). Therefore, the ice samples in our experimental simulations experience the same total fluence as the ice mantles during the typical lifetime of dense cores ($\sim 3 \times 10^{17}$ photons cm⁻² for a cloud lifetime of 10⁶ years) after 30 min of irradiation. At the same time, the UV flux experienced by the ice samples in the experiments is about four orders of magnitude higher than that present in low-illuminated PDRs.

As mentioned in Sect. 1, gas-phase abundances of CH₃OH in dense cores and PDRs where thermal desorption is inhibited cannot be reproduced by gas-phase chemical models, and solid chemistry followed by nonthermal desorption needs to be invoked. Methanol formation was not observed during irradiation of a pure ethanol ice sample, but it was formed in the H₂O:CH₄ ice irradiation experiments, accounting for $\sim 1\%$ of the total initial column density. However, photon-induced desorption of methanol was not observed in this second series of experiments, and therefore its abundance in these regions remains an open question in astrochemistry.

On the other hand, formaldehyde was formed in both series of experiments. Photochemidesorption of this species was detected with a yield of $\leq 6 \times 10^{-5}$ ($\frac{\text{molecules}}{\text{incident photon}}$) in the case of the pure ethanol ice experiments, and $\sim 4.4 \times 10^{-5}$ ($\frac{\text{molecules}}{\text{incident photon}}$) when the H₂O:CH₄ ice analogs were photoprocessed. The latter value (more accurate, and closer to the astrophysical scenario) could be used in gas-grain chemical models, taking photon-induced desorption from dust grains and subsequent gas-phase reactions into account, in order to test whether

photochemidesorption of formaldehyde as observed in this work is able to account for all the formaldehyde detected in low UV-field illuminated PDRs or if an additional source of formaldehyde is needed.

5. Conclusions

We have explored two UV-induced formation pathways and subsequent desorption for CH₃OH and H₂CO, which are two simple organic molecules that are ubiquitously detected in the ISM. Photoproduction of these species was searched for with an IR spectrometer during UV irradiation of the ice samples. Photon-induced desorption of several photoproducts was observed directly in the gas phase by means of mass spectrometry. Calibration of our QMS allowed us to quantify the photon-induced desorbing molecules and calculate desorption yields.

In a first series of experiments, a top-down approach to the formation of methanol and formaldehyde was used when studying the photodissociation of a pure ethanol ice. Seven photoproducts were detected: H₂O, CO, CO₂, CH₄, C₂H₆, H₂CO, and CH₃CHO. Photon-induced desorption of four of the photoproducts was observed during photoprocessing of the ice sample. The increasing desorption yield observed for H₂O, CO, and CH₄ suggests that the DIET mechanism was active for these species. In particular, the photon-induced desorption yield of water and methane reached constant values of $\leq 2.6 \times 10^{-4}$ ($\frac{\text{molecules}}{\text{incident photon}}$) and $\sim 3.3 \times 10^{-4}$ ($\frac{\text{molecules}}{\text{incident photon}}$), respectively, after a fluence of 1.8×10^{17} photons cm⁻², while that of carbon monoxide continued increasing, reaching a value of 1.5×10^{-3} ($\frac{\text{molecules}}{\text{incident photon}}$) after a total fluence of 7.2×10^{17} photons cm⁻². On the other hand, formaldehyde and/or ethane molecules were observed to photochemidesorb with a constant desorption yield of $\sim 6 \times 10^{-5}$ ($\frac{\text{molecules}}{\text{incident photon}}$) in case the QMS $m/z = 29$ signal was only due to H₂CO molecules.

In a second series of experiments, a bottom-up approach was explored, using a more realistic water-rich ice analog containing methane. Photoprocessing of H₂O:CH₄ ice samples with a 3:1 ratio led to a simpler photochemical network, and only four photoproducts were detected: CO, CO₂, CH₃OH, and H₂CO. Only CO and H₂CO were observed to desorb upon UV irradiation of the ice mixtures. The photon-induced desorption yield of carbon monoxide was found to increase during photoprocessing up to 4.9×10^{-4} ($\frac{\text{molecules}}{\text{incident photon}}$) after a total fluence of 7.2×10^{17} photons cm⁻², suggesting that the desorption was driven by the DIET mechanism. Photochemidesorption of formaldehyde was also detected, with a constant yield of $\sim 4.4 \times 10^{-5}$ ($\frac{\text{molecules}}{\text{incident photon}}$). These results were confirmed using H₂O:¹³CH₄ ice analogs.

Methanol was only formed during the second series of experiments, but no significant photon-induced desorption was observed. So far, there has been no experimental evidence of an efficient nonthermal desorption mechanism that explained

the gas-phase methanol abundances in dense cores and low UV-field illuminated PDRs, where thermal desorption from ice mantles is inhibited, and gas-phase chemical models fail to account for all the detected methanol. On the other hand, formaldehyde was photoproduced in both series of experiments. Photochemidesorption took place with a similar yield in both cases. While gas-phase chemical models are able to reproduce the formaldehyde abundances in dense cores, formation in the solid phase and subsequent desorption to the gas phase is needed in the case of low UV-field illuminated PDRs. The photon-induced desorption yield found in this work can be used in gas-grain chemical models to test that the observed column densities of formaldehyde in low UV-field illuminated PDRs can be explained by the proposed photon-induced formation and subsequent desorption process.

Acknowledgements. We are grateful to Javier Manzano-Santamaría for his support on the experiments. Special thanks go to Marcelino Agúndez for useful discussions. This research was financed by the Spanish MINECO under projects AYA2011-29375 and AYA2014-60585-P. R.M.D. benefited from a FPI grant from Spanish MINECO.

References

- Araya, E., Hofner, P., Goss, W. M., et al. 2007, *ApJS*, **170**, 152
- Bergman, P., Parise, B., Liseau, R., & Larsson, B. 2011, *A&A*, **527**, A39
- Bernstein, M. P., Sandford, S. A., Allamandola, L. J., Chang, S., & Scharberg, M. A. 1995, *ApJ*, **454**, 327
- Bernstein, M. P., Dworkin, J. P., Sandford, S. A., Cooper, G. W., & Allamandola, L. J. 2002, *Nature*, **416**, 401
- Bertin, M., Fayolle, E. C., Romanzin, C., et al. 2012, *Phys. Chem. Chem. Phys.*, **14**, 9929
- Bertin, M., Fayolle, E. C., Romanzin, C., et al. 2013, *ApJ*, **779**, 120
- Boogert, A. C. A., Pontoppidan, K. M., Knez, C., et al. 2008, *ApJ*, **678**, 985
- Boogert, A. C. A., Huard, T. L., Cook, A. M., et al. 2011, *ApJ*, **729**, 92
- Boogert, A. C. A., Gerakines, P. A., & Whittet, D. C. B. 2015, *ARA&A*, **53**, 541
- Bottinelli, S., Boogert, A. C. A., Bouwman, J., et al. 2010, *ApJ*, **718**, 1100
- Ceccarelli, C., Loinard, L., Castets, A., Tielens, A. G. G. M., & Caux, E. 2000, *A&A*, **357**, L9
- Cecchi-Pestellini, C., & Aiello, S. 1992, *MNRAS*, **258**, 125
- Charnley, S. B., Tielens, A. G. G. M., & Millar, T. J. 1992, *ApJ*, **399**, L71
- Chen, Y.-J., Chu, C.-C., Lin, Y.-C. et al. 2010, *Adv. Geosci.*, **25**, 259
- Chen, Y.-J., Chuang, K.-J., Muñoz Caro, G. M., et al. 2014, *ApJ*, **781**, 15
- Ciaravella, A., Muñoz Caro, G., Jiménez-Escobar, A. et al. 2010, *ApJ*, **722**, L45
- Cruz-Díaz, G. A., Muñoz Caro, G. M., Chen, Y.-J., & Yih, T.-S. 2014, *A&A*, **562**, A119
- Dartois, E. 2005, *Space Sci. Rev.*, **119**, 293
- Dartois, E., Geballe, T. R., Demyk, K., Ehrenfreund, P., & d'Hendecourt, L. 1999, *A&A*, **342**, L32
- d'Hendecourt, L. B., & Allamandola, L. J. 1986, *A&AS*, **64**, 453
- Ehrenfreund, P., Irvine, W., Becker, L., et al. 2002, *Rep. Prog. Phys.*, **65**, 1427
- Fayolle, E. C., Bertin, M., Romanzin, C., et al. 2011, *ApJ*, **739**, L36
- Fayolle, E. C., Bertin, M., Romanzin, C., et al. 2013, *A&A*, **556**, A122
- Fillion, J.-H., Fayolle, E., Michaut, X., et al. 2014, *Faraday Discuss.*, **168**, 533
- France, K., Andersson, B.-G., McCandliss, S. R., & Feldman, P. D. 2005, *ApJ*, **682**, 750
- Fuchs, G. W., Cuppen, H. M., Ioppolo, S., et al. 2009, *A&A*, **505**, 629
- Garrod, R. T., Park, I. H., aselli, P., & Herbst, E. 2006, *Faraday Discuss.*, **133**, 51
- Garrod, R. T., Wakelam, V., & Herbst, E. 2007, *A&A*, **467**, 1103
- Garrod, R. T., Weaver, S. L., & Herbst, E. 2008, *ApJ*, **682**, 283
- Geppert, W. D., Hamberg, M., Thomas, R. D., et al. 2006, *Faraday Discuss.*, **133**, 177
- Gerakines, P. A., Schutte, W. A., Greenberg, J. M., & van Dishoeck, E. F. 1995, *A&A*, **296**, 810
- Gerakines, P. A., Moore, M. H., & Hudson, R. L. 2001, *J. Geophys. Res.*, **106**, 33381
- Gibb, E. L., Whittet, D. C. B., Schutte, W. A. 2000, *ApJ*, **536**, 347
- Gibb, E. L., Whittet, D. C. B., Boogert, A. C. A., & Tielens, A. G. G. M. 2004, *ApJS*, **151**, 35
- Gredel, R., Lepp, S., Dalgarno, A., & Herbst, E. 1989, *ApJ*, **347**, 289
- Guzmán, V. V., Pety, J., Goicoechea, J. R., Gerin, M., & Roueff, E. 2011, *A&A*, **534**, A49
- Guzmán, V. V., Goicoechea, J. R., Pety, J., et al. 2013, *A&A*, **560**, A73
- Hagen, W. 1981, *Chem. Phys.*, **56**, 367
- Hiraoka, K., Ohashi, N., Kihara, Y., et al. 1994, *Chemp. Phys. Lett.*, **229**, 408
- Herbst, E., & van Dishoeck, E. F. 2009, *ARA&A*, **47**, 427
- Hiraoka, K., Sato, T., Sato, S., et al. 2002, *ApJ*, **577**, 265
- Hiraoka, K., Wada, A., Hidekazu, K., et al. 2005, *ApJ*, **620**, 542
- Hocuk, S., & Cazaux, S. 2015, *A&A*, **576**, A49
- Hudson, R. L., Moore, M. H. 1999, *Icarus*, **140**, 451
- Jenniskens, P., Baratta, G. A., Kouchi, A., et al. 1993, *A&A*, **273**, 583
- Kaiser, R. I., Jansen, P., Petersen, K., & Roessler, K. 1995, *Rev. Sci. Instr.*, **66**, 5226
- Keane, J. V., Tielens, A. G. G. M., Boogert, A. C. A. Schutte, W. A., & Whittet, D. C. B. 2001, *A&A*, **376**, 254
- Leurini, S., Parise, B., Schilke, P. Pety, J., & Roloffs, R. 2010, *A&A*, **511**, A82
- Loeffler, M. J., Baratta, G. A., Palumbo, M. E., Strazzulla, G., & Baragiola, R. A. 2005, *A&A*, **435**, 587
- Madzunkov, S. M., MacAskill, J. A., Chutjian, A. et al. 2009, *ApJ*, **697**, 801
- Madzunkov, S. M., MacAskill, J. A., Chutjian, A. et al. 2010, *ApJ*, **712**, 194
- Maret, S., Ceccarelli, C., Caux, E., et al. 2004, *A&A*, **416**, 577
- Martín-Doménech, R., Muñoz Caro, G. M., Bueno, J., & Goesmann, F. 2014, *A&A*, **564**, A8
- Martín-Doménech, R., Manzano-Santamaría, J., Muñoz Caro, G. M., et al. 2015, *A&A*, **584**, A14
- Moore, M. H., & Hudson, R. L. 1998, *Icarus*, **135**, 518
- Mumma, M. J., & Charnley, S. B., 2011, *ARA&A*, **49**, 471
- Muñoz Caro, G. M., & Dartois, E. 2009, *A&A*, **494**, 109
- Muñoz Caro, G. M., & Schutte, W. A. 2003, *A&A*, **412**, 121
- Muñoz Caro, G. M., Meierhenrich, U. J., Schutte, W. A., et al. 2002, *Nature*, **416**, 403
- Muñoz Caro, G. M., Jiménez-Escobar, A., Martín-Gago, J.Á., et al. 2010, *A&A*, **522**, A108
- Noble, J. A., Theule, P., Mispelaer, F., et al. 2012, *A&A*, **543**, A5
- Nuevo, M., Meierhenrich, U. J., Muñoz Caro, G. M., et al. 2006, *A&A*, **457**, 741
- Öberg, K. I., Fuchs, G. W., Zainab, A., et al. 2007, *ApJ*, **662**, L23
- Öberg, K. I., Garrod, R. T., van Dishoeck, E. F., & Linnartz, H. 2009, *A&A*, **504**, 891
- Öberg, K. I., Bottinelli, S., Jørgensen, J. K., & van Dishoeck, E. F. 2010, *ApJ*, **716**, 825
- Öberg, K. I., Boogert, A. C. A., Pontoppidan, K. M., et al. 2011, *ApJ*, **740**, 109
- Öberg, K. I., Fayolle, E. C., Reiter, J. B., & Cyganowski, C. 2014, *Faraday Discuss.*, **168**, 81
- Pety, J., Gratier, P., Guzmán, V., et al. 2012, *A&A*, **548**, A68
- Pontoppidan, K. M., Boogert, A. C. A., Fraser, H. J. et al. 2008, *ApJ*, **678**, 1005
- Rakhovskaia, O., Wiethoff, P., & Feulner, P. 1995, *Nucl. Inst. Meth. Phys. Res. B*, **101**, 169
- Schriver, A., Schriver-Mazzuoli, L., Ehrenfreund, P., & d'Hendecourt, L. 2007, *Chem. Phys.* **334**, 128
- Schutte, W. A., Gerakines, P. A., Geballe, T. R., van Dishoeck, E. F., & Greenberg, J. M. 1996, *A&A*, **309**, 633
- Schutte, W. A., Boogert, A. C. A., Tielens, A. G. G. M., et al. 1999, *A&A*, **343**, 966
- Shen, C. J., Greenberg, J. M., Schutte, W. A., & van Dishoeck, E. F. 2004, *A&A*, **415**, 203
- Smith, I. W. M., Herbst, E., & Chang, Q. 2004, *MNRAS*, **350**, 323
- Sutton, E. C., Peng, R., Danchi, W. C., et al. 1995, *ApJS*, **97**, 455
- Tielens, A. G. G. M., & Hagen, W. 1982, *A&A*, **114**, 245
- Tielens, A. G. G. M., & Whittet, D. C. B. 1997, in *Molecules in Astrophysics: Probe and Processes*, ed. E. F. van Dishoeck (Dordrecht: Kluwer), 45
- Wada, A., Mochizuki, N., & Hiraoka, K. 2006, *ApJ*, **644**, 300
- Watanabe, N., & Kouchi, A. 2002, *ApJ*, **571**, L173
- Watanabe, N., Shikari, T., & Kouchi, A. 2003, *ApJ*, **588**, L121
- Watanabe, N., Mouri, O., Nagaoka, A., Chigai, T., & Kouchi, A. 2007, *ApJ*, **668**, 1001
- Wootten, A., Mangum, J., & Barsony, M. 1996, *BAAS*, **28**, 1415
- Yamamoto, S., Beniya, A., Mukai, K., Yamashita, Y., & Yoshinobu, J. 2004, *Chem. Phys. Lett.*, **388**, 384
- Young, K. E., Lee, J., Evans, II, N. J., Goldsmith, P. F., & Doty, S. D. 2004, *ApJ*, **614**, 252